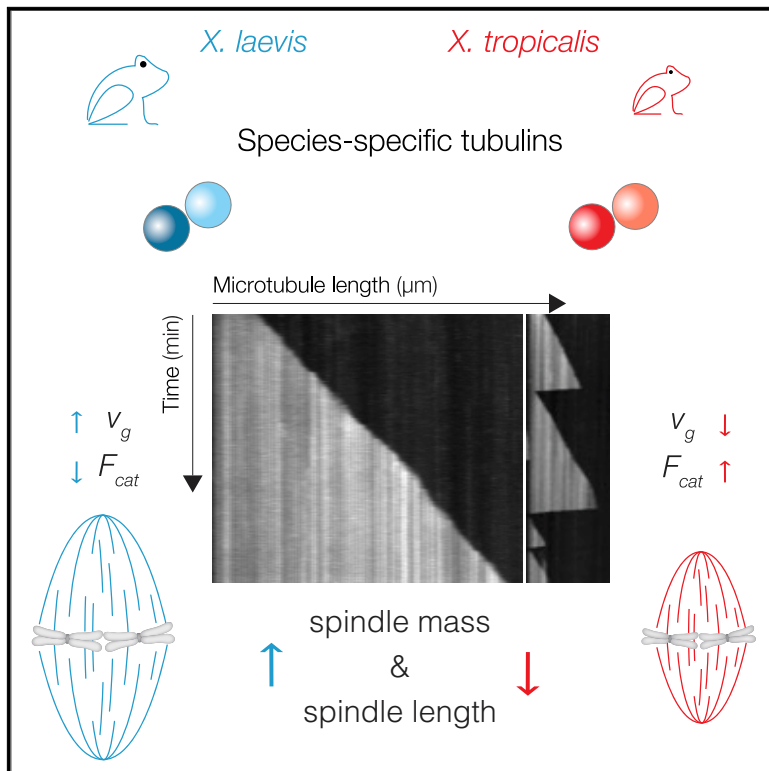# Differences in Intrinsic Tubulin Dynamic Properties Contribute to Spindle Length Control in *Xenopus* Species

Graphical Abstract

Authors

William G. Hirst, Abin Biswas,
Kishore K. Mahalingan, Simone Reber

Correspondence

simone.reber@iri-lifesciences.de

In Brief

Hirst et al. show that microtubules assembled from tubulins of two closely related frogs, *Xenopus laevis* and *X. tropicalis*, display different dynamic instability parameters *in vitro*. Computational simulations and spindle assembly assays show that differences in tubulin-dependent microtubule dynamics are sufficient to tune spindle mass and length.

Highlights

- *Xl* microtubules combine fast growth and infrequent catastrophes when compared to *Xt*

- Microtubule length can be modified by titrating different tubulins

- Spindle mass and length are modulated differently by species-specific tubulins

CellPress

Report

Differences in Intrinsic Tubulin Dynamic Properties Contribute to Spindle Length Control in *Xenopus* Species

William G. Hirst,[1,2,3] Abin Biswas,[1,3] Kishore K. Mahalingan,[4] and Simone Reber[1,3,5,6,*]
[1]IRI Life Sciences, Humboldt-Universität zu Berlin, 10115 Berlin, Germany
[2]Research School of Biology, The Australian National University, Canberra, ACT 2600, Australia
[3]Marine Biological Laboratory, Woods Hole, MA 02543, USA
[4]Cell Biology and Biophysics Unit, NINDS, NIH, Bethesda, MD 20892, USA
[5]University of Applied Sciences Berlin, 13353 Berlin, Germany
[6]Lead Contact
*Correspondence: simone.reber@iri-lifesciences.de
https://doi.org/10.1016/j.cub.2020.03.067

SUMMARY

The function of cellular organelles relates not only to their molecular composition but also to their size. However, how the size of dynamic mesoscale structures is established and maintained remains poorly understood [1–3]. Mitotic spindle length, for example, varies several-fold among cell types and among different organisms [4]. Although most studies on spindle size control focus on changes in proteins that regulate microtubule dynamics [5–8], the contribution of the spindle's main building block, the $\alpha\beta$-tubulin heterodimer, has yet to be studied. Apart from microtubule-associated proteins and motors, two factors have been shown to contribute to the heterogeneity of microtubule dynamics: tubulin isoform composition [9, 10] and post-translational modifications [11]. In the past, studying the contribution of tubulin and microtubules to spindle assembly has been limited by the fact that physiologically relevant tubulins were not available. Here, we show that tubulins purified from two closely related frogs, *Xenopus laevis* and *Xenopus tropicalis*, have surprisingly different microtubule dynamics *in vitro*. *X. laevis* microtubules combine very fast growth and infrequent catastrophes. In contrast, *X. tropicalis* microtubules grow slower and catastrophe more frequently. We show that spindle length and microtubule mass can be controlled by titrating the ratios of the tubulins from the two frog species. Furthermore, we combine our *in vitro* reconstitution assay and egg extract experiments with computational modeling to show that differences in intrinsic properties of different tubulins contribute to the control of microtubule mass and therefore set steady-state spindle length.

RESULTS

Xenopus laevis Microtubules Combine Fast Growth and Infrequent Catastrophes *In Vitro*

In very large cells, like *X. laevis* eggs (~1,200 μm), spindle size approaches an upper limit [12], which is species dependent. *X. tropicalis* spindles are ~30% shorter than *X. laevis* spindles [13] (Figure 1A). Extracts of unfertilized eggs and embryos of the two related frog species have proven valuable to elucidate key factors of both spindle scaling [14, 15] as well as spindle length control [5, 13, 16]. For example, the microtubule severing enzyme katanin (Figure 1A) is differentially regulated in *X. laevis* and *X. tropicalis*. A single phosphorylation site missing from *X. tropicalis* katanin increases its activity and has been reported to be largely responsible for the observed difference in spindle length [5]. To study the potential contribution of tubulin to setting initial spindle length, we purified tubulin [17] from cytostatic factor (CSF) extracts prepared from unfertilized eggs from *X. laevis* and *X. tropicalis* frogs (Figure S1A). Importantly, the purified tubulins were free of contaminating microtubule-associated

proteins (MAPs) and motors (Figure S1B; Table S1) and assembly competent (Figure S1C). Using a total internal reflection microscopy (TIRFM)-based *in vitro* assay [18], we measured microtubule growth from GMPCPP-stabilized microtubule seeds. Surprisingly, we found that *X. laevis* microtubules nucleated from GMPCPP templates at tubulin concentrations as low as 1.5 μM. In contrast, robust nucleation from templates was observed only at 6 μM tubulin for *X. tropicalis* microtubules (Figure S1D). This nucleation threshold is below that of *Bos taurus* tubulin (purified from bovine brain) at around 9 μM (Figure S1D) [10, 19]. Kymographs of dynamic microtubules showed that *X. laevis* microtubules not only grew fast, they also had very long lifetimes (Figure 1B). This is consistent with faster growth correlating with longer lifetimes [9, 20]. Quantifying and comparing parameters of microtubule dynamic instability, we found *X. laevis* microtubules to have an increased polymerization velocity (1.92 ± 0.02 μm/min versus 0.96 ± 0.02 μm/min; Figure 1C) and a lower catastrophe frequency (<0.00015 s^{-1} versus 0.0044 ± 0.00076 s^{-1}; Figure 1E) when compared to *X. tropicalis* microtubules. In the rare event of a *X. laevis* microtubule
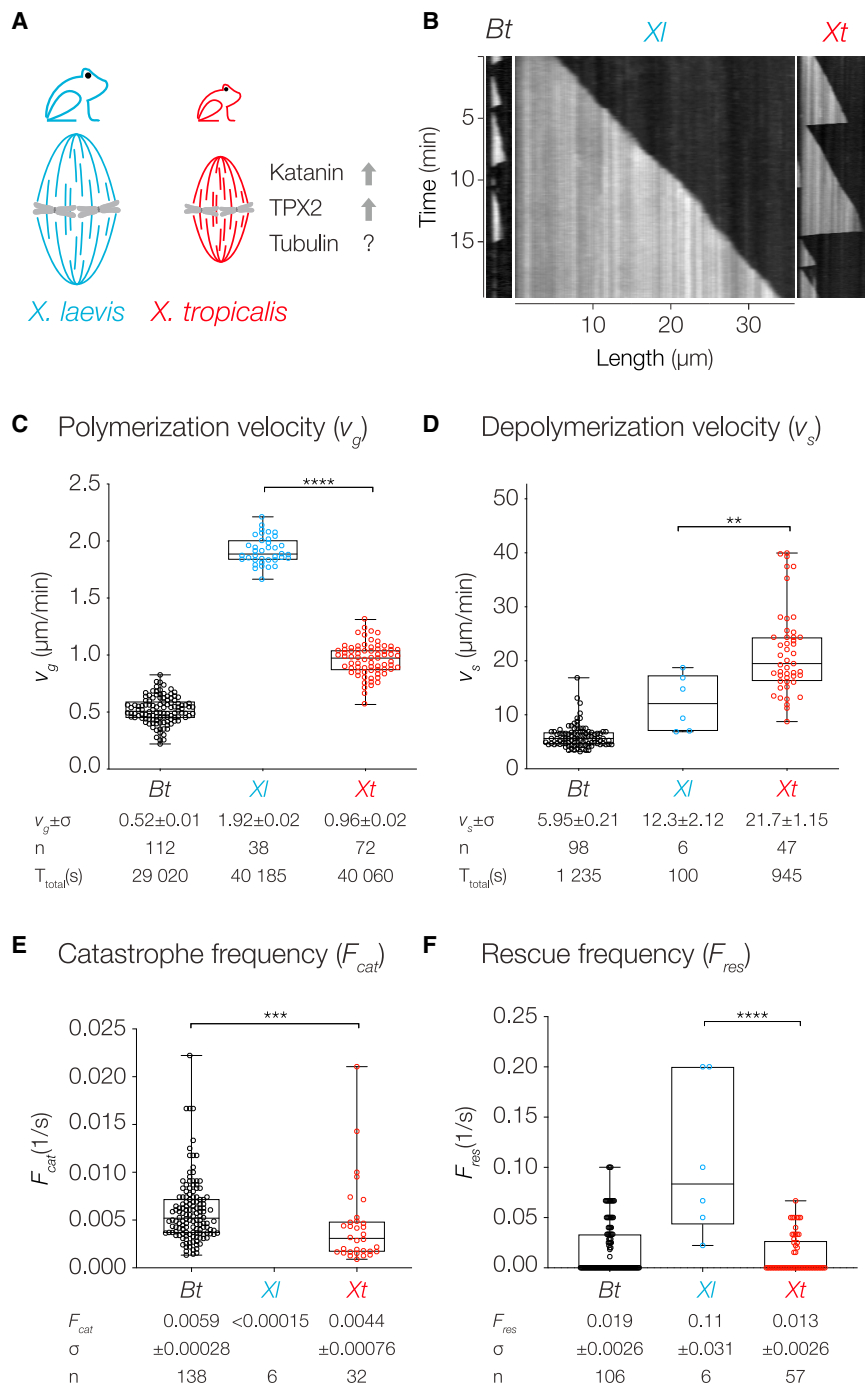
Figure 1. *Xenopus laevis* Microtubules Combine Fast Growth and Infrequent Catastrophes *In Vitro*

(A) Intrinsic spindle length differs between the two related frogs *Xenopus laevis* (*Xl*) and *tropicalis* (*Xt*). Although a few factors are known to differentially control spindle length in these systems, the role of tubulin remains unknown.

(B) Representative TIRF kymographs showing dynamic *Bt* (*Bos taurus*), *Xl*, and *Xt* microtubules at 9 μM tubulin.

(C–F) Parameters of dynamic instability. All values were obtained from measurements of microtubules pooled over at least 3 independent experiments, and all p values are calculated with the Mann-Whitney test.

(C) *Bt* microtubules grow at 0.52 ± 0.01 μm/min (14.0 ± 0.3 dimers/s), *Xl* microtubules at 1.92 ± 0.02 μm/min (51.9 ± 0.5 dimers/s), and *Xt* microtubules at 0.96 ± 0.02 μm/min (25.9 ± 0.5 dimers/s) with $p_{(Xl, Xt)} < 0.0001$.

(D) *Bt* microtubules depolymerize at 5.95 ± 0.21 μm/min (161 ± 5.67 dimers/s), *Xl* microtubules at 12.3 ± 2.12 μm/min (332 ± 57.3 dimers/s), and *Xt* microtubules at 21.7 ± 1.15 μm/min (587 ± 31.2 dimers/s) with $p_{(Xl, Xt)} = 0.0039$.

(E) Catastrophe frequencies are reported as the inverse of microtubule lifetimes. *Xl* microtubules catastrophe very rarely (<0.00015 s^{-1}) although *Xt* microtubules catastrophe at 0.0044 ± 0.00076 s^{-1} with $p_{(Bt, Xt)} = 0.0002$.

(F) Rescue frequencies are reported as the inverse of the duration of each depolymerization event. Events without a rescue are given a value of zero. *Xl* microtubules rescue at 0.11 ± 0.031 s^{-1} and *Xt* microtubules at 0.013 ± 0.0026 s^{-1}, with $p_{(Xl, Xt)} < 0.0001$. Total time (T_{total}) of observed microtubule growth and shrinkage, SEM (σ), and number of events (n) are indicated. For the modified box-and-whiskers plots, the boxes range from 25th to 75th percentile, the whiskers span the range, and the horizontal line marks the median value.

See also Figure S1.

such variability in polymerization properties is isoform composition encoded by distinct tubulin genes. *X. laevis* and *tropicalis* both have several α-tubulin and β-tubulin isoforms (Figure S2A). Sequence identity between isoforms is very high, ranging from 96.1% (A8) up to 100% (B5; Figure S2B), making the identification of individual isoforms challenging. However, mass spectrometric analysis indicates that our purified tubulin preparations contain two major α-tubulin isoforms, A1 and AL3 (Figures 2A and S2A), and one major β-tubulin isoform (Figures 2B and S2A), which is B4B. This suggests that the tubulin populations are qualitatively similar in isoform composition. In addition to genetic diversity, tubulins also are functionalized with diverse post-translational modifications (PTMs), such as acetylation, polyglutamylation, phosphorylation, and (de-)tyrosination (as reviewed in [21–23]). To test whether the differences in microtubule dynamics we observe between

undergoing catastrophe, it rescued with a higher frequency (0.11 ± 0.031 s^{-1} versus 0.013 ± 0.0026 s^{-1}; Figure 1F). Taken together, our results demonstrate that *X. laevis* microtubules combine very fast growth with long lifetimes *in vitro* when compared to *X. tropicalis* microtubules.
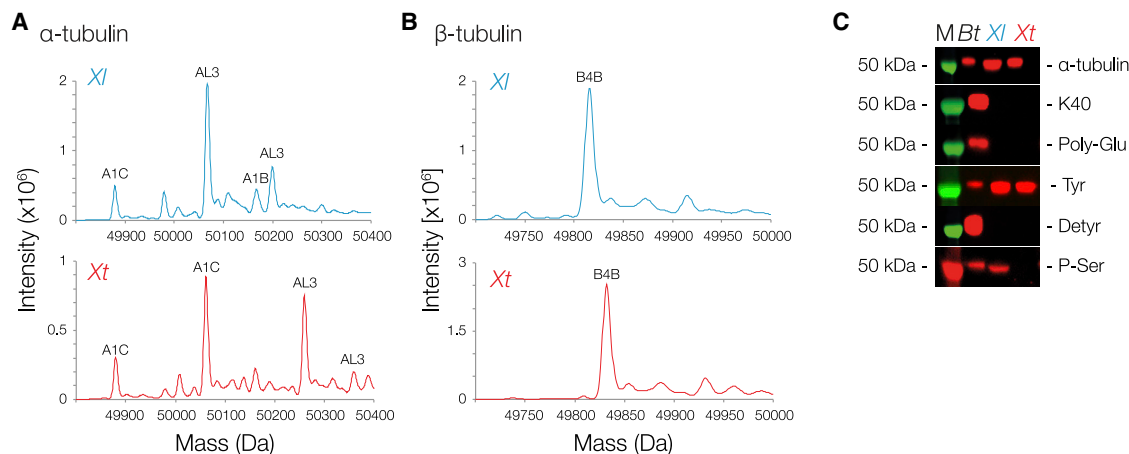
Xenopus laevis and *tropicalis* Tubulin Populations Differ in Their Phosphorylation Pattern

How can such a significant difference in microtubule dynamics be encoded in a single dimer of αβ-tubulin? One source of

Figure 2. *Xenopus laevis* and *tropicalis* Tubulin Populations Differ in a Phosphorylation
(A and B) Mass spectra of purified *Xl* and *Xt* α-tubulin (A) and β-tubulin (B). Individual tubulin isoforms are labeled in each spectrum.
(C) Western blots probing post-translational modifications found in purified *Bt*, *Xl*, and *Xt* tubulin. α-tubulin is a loading control, K40 recognizes acetylated lysine at position 40 of α-tubulin, Poly-Glu recognizes epitopes containing acidic residues modified with a chain of at least 2 glutamyl residues, Tyr recognizes the C-terminal EEY epitope of tyrosinated tubulin, Detyr recognizes the detyrosinated C terminus of α-tubulin, and P-Ser is pan specific for phosphorylated serine residues.
See also Figure S2.

X. laevis and *X. tropicalis* stem from differential post-translational modifications, we used western blot analysis. In contrast to bovine tubulin, which is heavily post-translationally modified, frog tubulin carries almost no post-translational modifications (Figure 2C). However, we find that *B. taurus* and *X. laevis* tubulin are phosphorylated although *X. tropicalis* tubulin is not (Figures 2C and S2D). To show that indeed phosphorylation is responsible for the observed differences in microtubule dynamics, we wanted to dephosphorylate *X. laevis* tubulin. Unfortunately, none of the tested phosphatases (bacteriophage lambda phosphatase, alkaline phosphatase, and human PP2A) was able to dephosphorylate purified *X. laevis* tubulin *in vitro* (Figure S2E). Although we were unable to show that phosphoregulation is the mechanism to differentially regulate microtubule dynamics, our data show that tubulin isoforms purified from eggs are qualitatively very similar in the two frog species.

Microtubule Length Can Be Modulated by Titrating Tubulin Sources

Differential microtubule dynamics are a mechanism by which spindles can achieve scaling with cell volume [24, 25]. In addition, theoretical arguments have shown that spindle mass and size are controlled by the balance between microtubule turnover and nucleation [26–28]. Based on the measured differences in dynamic parameters, we predicted that, at steady state (see STAR Methods), *X. laevis* microtubule length and mass should be higher than *X. tropicalis* microtubule mass. Indeed, the average length of a *X. laevis* microtubule was 36.1 ± 0.66 μm, 11.5 ± 0.65 μm for *X. tropicalis*, and 1.79 ± 0.17 μm for *B. taurus* at 9 μM tubulin (Figures S3A–S3C). Assuming that 1 μm of microtubule polymer contains 178.75 MDa of tubulin [29], we found that significantly more *X. laevis* tubulin was in the polymer state ($6,450 \pm 118$ MDa) when compared to *X. tropicalis* ($2,060 \pm 116$ MDa) and *B. taurus* (320 ± 30 MDa; Figures 3A and 3B). Intriguingly, when mixing *X. laevis* and *tropicalis*

tubulin, the microtubule growth velocity (Figure 3C), the average microtubule length (7.6 ± 0.78 μm at 6 μM), and the polymer mass (Figure 3D) increased with the proportion of *X. laevis* tubulin. In extracts, however, microtubule dynamics will be influenced by MAPs and motors. To show that *X. laevis* and *tropicalis* tubulin exhibit different microtubule dynamics in a physiological context, we measured microtubule growth in the two extract systems (Figure 3E). In *X. laevis* extracts, microtubules grow about 20% faster (21.83 ± 2.76 μm/min) than in *X. tropicalis* extracts (17.61 ± 3.25 μm/min). This is comparable to what has been measured for individual microtubules nucleated by centrosomes (18.5 ± 8.8 μm/min for *X. laevis* and 14.7 ± 4.4 μm/min for *X. tropicalis*) [13]. Furthermore, these data are consistent with the observation that mixing *X. laevis* and *tropicalis* extracts leads to spindles with an intermediate length [13]. In conclusion, our results show that the fast growth and infrequent catastrophes of *X. laevis* microtubules lead to longer microtubules and thus a higher microtubule mass at steady state when compared to *X. tropicalis*.

Spindle Mass and Length Scale with Tubulin Source and Tubulin Concentration

To show that indeed intrinsic tubulin properties contribute to setting spindle length, the classic experiment would be a depletion/add-back experiment, i.e., deplete tubulin from the extract of one *Xenopus* species and add back tubulin from the other species. Therefore, we tried to deplete endogenous tubulin from *X. laevis* egg extracts, add back *X. tropicalis* tubulin, and assemble spindles. However, we and others (Heald lab and Good lab, personal communication) did not succeed in significantly depleting tubulin from extracts. Although we successfully pulled down tubulin (Figure S4A), we were not able to significantly reduce the extract tubulin concentration (Figure S4B). Therefore, we decided to perform the depletion and add-back experiment *in silico* using the cytoskeletal simulation software
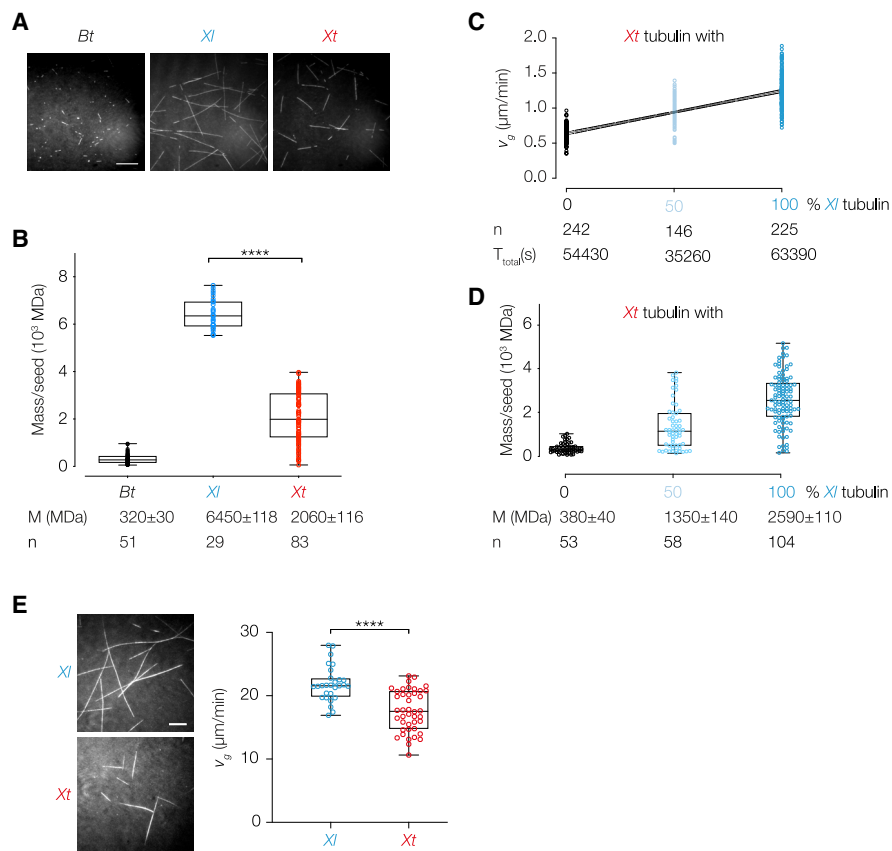
Figure 3. Microtubule Length Can Be Modulated by Titrating Tubulin Sources

(A) Representative TIRF images of microtubules polymerized from *Bt*, *Xl*, and *Xt* tubulin at 9 μM at steady state. Scale bar represents 15 μm.

(B) Mean microtubule mass per seed was calculated by measuring the length of each microtubule grown per seed (total number of measured seeds [n] indicated) and converting length to mass by assuming that one micrometer of microtubule polymer contains 178.75 MDa of tubulin [29]. Mass per seed values were pooled across at least 4 independent experiments for each species. Mean microtubule mass per seed for *Bt*, *Xl*, and *Xt* microtubules were 320 ± 30 MDa, 6,450 ± 118 MDa, and 2,060 ± 116 MDa, respectively, with $p_{(Xl, Xt)} < 0.0001$ (Mann-Whitney test).

(C) Growth rates were measured from microtubules assembled from *Xl* tubulin, *Xt* tubulin, and a 50/50 mixture at a final concentration of 6 μM. *Xt* microtubules grew at 0.63 ± 0.006 μm/min, mixed microtubules grew at 0.96 ± 0.015 μm/min, and *Xl* microtubules grew at 1.24 ± 0.015 μm/min. The linear regression is displayed with the 95% confidence interval.

(D) Microtubule mass per seed was calculated for single-species and mixed microtubules at 6 μM as in (C). Mean microtubule masses for *Xt*, mixed, and *Xl* microtubules were 380 ± 40 MDa, 1,350 ± 140 MDa, and 2,590 ± 110 MDa, respectively, with $p_{(Xt, Mix)}$, $p_{(Mix, Xl)}$, and $p_{(Xt, Xl)} < 0.0001$.

(E) Representative TIRF images of microtubules grown in *Xl* or *Xt* extracts. Scale bar represents 10 μm. Microtubule growth rates in extract were calculated as in Figure 1C. *Xl* and *Xt* microtubules grew at 21.8 ± 2.8 μm/min and 17.6 ± 3.2 μm/min, respectively, with $p < 0.0001$ (Mann-Whitney). Values were obtained from measurements pooled over at least two independent experiments.

See also Figure S3.

Cytosim (http://www.cytosim.org) [5, 16, 30]. First, we reproduced the differences in wild-type spindle length and microtubule mass (Figure 4A) reported for *X. laevis* and *X. tropicalis* [5, 16]. Next, we performed an *in silico* depletion and add-back experiment: we modeled either the *X. laevis* (Figure S4C) or *X. tropicalis* (Figure S4D) extract environment and provided our experimentally determined microtubule polymerization velocities for *X. laevis* and *tropicalis* microtubules (for parameters, see STAR Methods and Tables S2 and S3). The increase in *X. laevis* polymerization velocity was sufficient to significantly increase spindle length (Figures S4E and S4G) and spindle mass (Figures S4F and S4H). An alternative way to test the contribution of tubulins to setting spindle length would be the addition of different tubulin species to preassembled, steady-state spindles. We therefore modified the simulation in that we increased the basic microtubule polymerization velocity by the different polymerization velocities measured *in vitro* (for parameters, see Table S4). Plugging in *X. laevis* polymerization velocity led to a greater increase in spindle length than *X. tropicalis* polymerization velocity (Figure 4B). These findings support the idea that an increased microtubule growth velocity is sufficient to increase spindle mass. This is consistent with data showing that an increase in microtubule growth velocity increases *Xenopus* spindle length [7, 26]. Similar observations were made in *C. elegans* and *Paracentrotus lividus* [24], where the growth rate of spindle microtubules is the primary parameter that decreases proportionally to cell volume and spindle size during early development. Next, to experimentally test whether
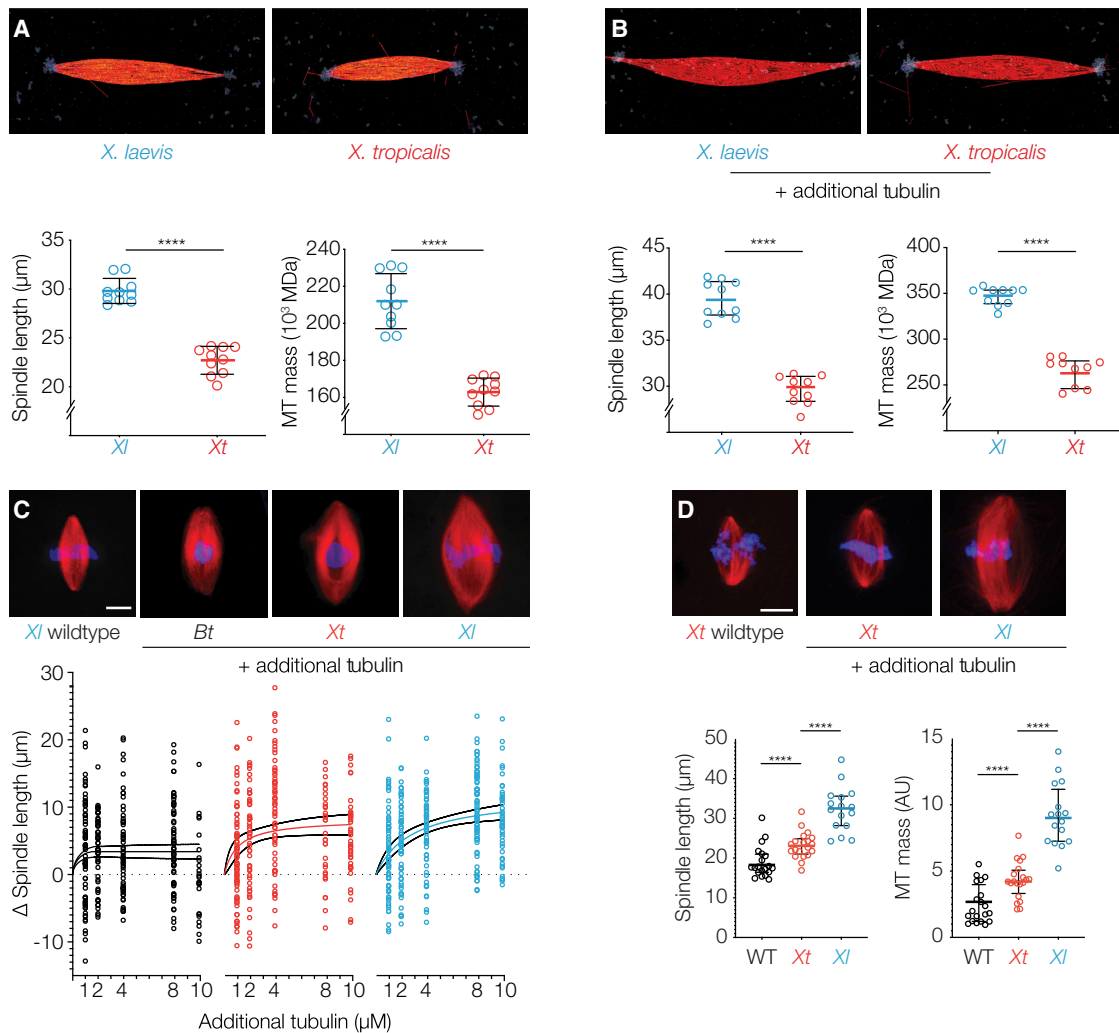
Figure 4. Spindle Length and Mass Scale with Tubulin Source and Tubulin Concentration

(A) Representative images of spindle simulations using the dynamic instability parameters of microtubules nucleated in *Xl* and *Xt* extracts [5, 13]. *Xl* spindles are longer than *Xt* spindles (29.8 ± 1.3 μm versus 22.7 ± 1.4 μm) with a higher spindle mass (212 ± 13.9 × 10³ MDa versus 163 ± 7.5 × 10³ MDa). Cytosim parameter values are summarized in Table S2.

(B) Simulations of spindles with additional tubulin (+8 μM). *Xl* spindles are longer than *Xt* spindles (39.8 ± 1.8 μm versus 29.6 ± 1.4 μm) with a higher spindle mass (347 ± 9.1 × 10³ MDa versus 265 ± 14.5 × 10³ MDa). Cytosim parameter values are summarized in Table S4.

(C) Representative images of steady-state spindles assembled in *Xl* egg extract after the addition of 8 μM tubulin purified from different sources (*Bt*, *Xl*, and *Xt*). Microtubules are shown in red and DNA in blue. Scale bar represents 10 μm. Quantification of normalized differences in spindle length. Each data point represents an individual spindle (n = 40–60 spindles). The bold line indicates a non-linear curve fit of the data. The addition of 10 μM *Xl* tubulin leads to longer spindles (33.8 ± 5.6 μm) than the addition of *Xt* tubulin (31.3 ± 6.1 μm) or *Bt* tubulin (25.8 ± 6.3 μm).

(D) Representative images of steady-state spindles assembled in *Xt* egg extract (wild type 18.9 ± 3.9 μm) and spindles after the addition of 8 μM tubulin purified from either *Xt* or *Xl* egg extracts. Microtubules are shown in red and DNA in blue. Scale bar represents 10 μm. Quantification of spindle length and mass is shown, and each data point represents an individual spindle (n = 20 spindles). The addition of *Xl* tubulin leads to longer spindles with a higher mass (32.3 ± 5.6 μm; 9.2 ± 2.3 a.u.) than the addition of *Xt* tubulin (23.2 ± 3.3 μm; 4.3 ± 1.4 a.u.). Student's t test with Welch's correction is shown. Black bar and line indicate mean and standard deviation.

****p < 0.0001, ***p < 0.001, and *p < 0.05. See also Figure S4.

Xenopus tubulins would affect spindle length and mass, we pre-assembled spindles in *X. laevis* egg extracts and added increasing amounts of tubulin from *B. taurus*, *X. tropicalis*, and *X. laevis* (Figure 4C). Although the addition of *B. taurus* tubulin had no significant effect on spindle length (−0.08%, as previously reported in [14]) and mass (Figure S4I), the addition of *X. tropicalis* and *X. laevis* tubulin increased spindle length by

21% and by 31%, respectively (Figure 4C). Similarly, we assembled spindles in *X. tropicalis* egg extracts and added 8 μM of *X. tropicalis* or *X. laevis* tubulin (Figure 4D). The addition of *X. laevis* tubulin led to a 70% increase in spindle length (wild-type spindles: 18.9 ± 3.9 μm; *X. laevis* spindles: 32.3 ± 5.6 μm) although the addition of *X. tropicalis* tubulin lead to a 23% increase in spindle length (23.2 ± 3.3 μm). These data show that

additional tubulin can increase spindle mass and length. Importantly, tubulin biochemistry and its inherent consequences for dynamic instability are essential to setting steady-state microtubule mass and thus spindle length.

DISCUSSION

Although previous studies of spindle size control and scaling have focused on microtubule-associated proteins and motors that regulate microtubule dynamics [5–8, 24–26], we addressed here the question of whether differences in tubulin itself can contribute to setting spindle length. We show that *X. laevis* microtubules grow faster and have longer lifetimes and an increased length at steady state when compared to *X. tropicalis* microtubules *in vitro*. Although the mass spectra of the two tubulins purified from frog eggs are qualitatively very similar, our data suggest that the difference in microtubule dynamics might stem from phosphorylation(s) present in *X. laevis*, but not in *X. tropicalis*, tubulin. Unfortunately, we were not able to dephosphorylate *X. laevis* tubulin *in vitro*. Indeed, it has been reported previously that tubulin is resistant to a variety of phosphatases [31]. However, phosphoregulation seems to be a reoccurring mechanism to set spindle length operating across several frog species [5, 6, 8]. Future studies will need to show whether indeed phosphorylation is responsible for the observed differences in microtubule dynamics. Although recent advances in understanding the role of individual tubulin isoforms or of specific tubulin post-translational modifications were made possible by using recombinant tubulins [32, 33], we here study a physiologically relevant mixture of tubulins. Therefore, in future studies, we will need to first understand the relative contribution of individual isoforms to the overall tubulin population and whether tubulin post-translational modifications are isoform specific before being able to fully reconstitute complex tubulin populations *in vitro*. Whether or not tubulin isoforms and their post-translational modifications are regulated to control spindle size during early developmental or differentiation remains an exciting perspective for future experiments. Prospective studies on tubulin populations purified from different species, cell types, or (malignantly) transformed cells promise to reveal new connections between tubulin intrinsic dynamic properties, spindle size, and the spindle's fundamental biological function.

STAR★METHODS

Detailed methods are provided in the online version of this paper and include the following:

- KEY RESOURCES TABLE
- LEAD CONTACT AND MATERIALS AVAILABILITY
- EXPERIMENTAL MODEL AND SUBJECT DETAILS
- METHOD DETAILS
  - Purification of *Xenopus* egg tubulin
  - Tubulin activity measurements
  - Spindle assembly reactions, imaging, and analysis
  - Depletion / add-back experiments and pull-down assays
  - Antibodies
  - TIRF assays, image acquisition, and data processing
  - Simulation
  - Mass spectrometry
  - Phosphatase assays
- QUANTIFICATION AND STATISTICAL ANALYSIS
- DATA AND CODE AVAILABILITY

SUPPLEMENTAL INFORMATION

Supplemental Information can be found online at https://doi.org/10.1016/j.cub.2020.03.067.

AUTHOR CONTRIBUTIONS

W.G.H. and S.R. conceived the project. W.G.H. and A.B. purified the tubulin. A.B. performed the simulations and the spindle assembly experiments. K.K.M. performed the mass spectrometry. W.G.H. performed all other experiments and analyzed the data. S.R. wrote the paper with input from all authors.

DECLARATION OF INTERESTS

The authors declare no competing interests.

REFERENCES

1. Mitchison, T.J., Ishihara, K., Nguyen, P., and Wühr, M. (2015). Size scaling of microtubule assemblies in early Xenopus embryos. Cold Spring Harb. Perspect. Biol. *7*, a019182.

2. Reber, S., and Goehring, N.W. (2015). Intracellular scaling mechanisms. Cold Spring Harb. Perspect. Biol. *7*, a019067.

3. Heald, R., and Gibeaux, R. (2018). Subcellular scaling: does size matter for cell division? Curr. Opin. Cell Biol. *52*, 88–95.

4. Crowder, M.E., Strzelecka, M., Wilbur, J.D., Good, M.C., von Dassow, G., and Heald, R. (2015). A comparative analysis of spindle morphometrics across metazoans. Curr. Biol. *25*, 1542–1550.

5. Loughlin, R., Wilbur, J.D., McNally, F.J., Nédélec, F.J., and Heald, R. (2011). Katanin contributes to interspecies spindle length scaling in Xenopus. Cell *147*, 1397–1407.

6. Helmke, K.J., and Heald, R. (2014). TPX2 levels modulate meiotic spindle size and architecture in Xenopus egg extracts. J. Cell Biol. *206*, 385–393.

7. Milunovic-Jevtic, A., Jevtic, P., Levy, D.L., and Gatlin, J.C. (2018). In vivo mitotic spindle scaling can be modulated by changing the levels of a single protein: the microtubule polymerase XMAP215. Mol. Biol. Cell *29*, 1311–1317.

8. Miller, K.E., Session, A.M., and Heald, R. (2019). Kif2a scales meiotic spindle size in *Hymenochirus boettgeri*. Curr. Biol. *29*, 3720–3727.E5.

9. Vemu, A., Atherton, J., Spector, J.O., Moores, C.A., and Roll-Mecak, A. (2017). Tubulin isoform composition tunes microtubule dynamics. Mol. Biol. Cell *28*, 3564–3572.

10. Chaaban, S., Jariwala, S., Hsu, C.T., Redemann, S., Kollman, J.M., Müller-Reichert, T., Sept, D., Bui, K.H., and Brouhard, G.J. (2018). The structure and dynamics of C. elegans tubulin reveals the mechanistic basis of microtubule growth. Dev. Cell *47*, 191–204.e8.

11. Xu, Z., Schaedel, L., Portran, D., Aguilar, A., Gaillard, J., Marinkovich, M.P., Théry, M., and Nachury, M.V. (2017). Microtubules acquire resistance from mechanical breakage through intralumenal acetylation. Science *356*, 328–332.

12. Wühr, M., Chen, Y., Dumont, S., Groen, A.C., Needleman, D.J., Salic, A., and Mitchison, T.J. (2008). Evidence for an upper limit to mitotic spindle length. Curr. Biol. *18*, 1256–1261.

13. Brown, K.S., Blower, M.D., Maresca, T.J., Grammer, T.C., Harland, R.M., and Heald, R. (2007). Xenopus tropicalis egg extracts provide insight into scaling of the mitotic spindle. J. Cell Biol. *176*, 765–770.

14. Good, M.C., Vahey, M.D., Skandarajah, A., Fletcher, D.A., and Heald, R. (2013). Cytoplasmic volume modulates spindle size during embryogenesis. Science *342*, 856–860.

15. Hazel, J., Krutkramelis, K., Mooney, P., Tomschik, M., Gerow, K., Oakey, J., and Gatlin, J.C. (2013). Changes in cytoplasmic volume are sufficient to drive spindle scaling. Science *342*, 853–856.

16. Loughlin, R., Heald, R., and Nédélec, F. (2010). A computational model predicts Xenopus meiotic spindle organization. J. Cell Biol. *191*, 1239–1249.

17. Widlund, P.O., Podolski, M., Reber, S., Alper, J., Storch, M., Hyman, A.A., Howard, J., and Drechsel, D.N. (2012). One-step purification of assembly-competent tubulin from diverse eukaryotic sources. Mol. Biol. Cell *23*, 4393–4401.

18. Gell, C., Bormuth, V., Brouhard, G.J., Cohen, D.N., Diez, S., Friel, C.T., Helenius, J., Nitzsche, B., Petzold, H., Ribbe, J., et al. (2010). Microtubule dynamics reconstituted in vitro and imaged by single-molecule fluorescence microscopy. Methods Cell Biol. *95*, 221–245.

19. Wieczorek, M., Bechstedt, S., Chaaban, S., and Brouhard, G.J. (2015). Microtubule-associated proteins control the kinetics of microtubule nucleation. Nat. Cell Biol. *17*, 907–916.

20. Ti, S.C., Pamula, M.C., Howes, S.C., Duellberg, C., Cade, N.I., Kleiner, R.E., Forth, S., Surrey, T., Nogales, E., and Kapoor, T.M. (2016). Mutations in human tubulin proximal to the kinesin-binding site alter dynamic instability at microtubule plus-and minus-ends. Dev. Cell *37*, 72–84.

21. Amargant, F., Barragan, M., Vassena, R., and Vernos, I. (2019). Insights of the tubulin code in gametes and embryos: from basic research to potential clinical applications in humans. Biol. Reprod. *100*, 575–589.

22. Roll-Mecak, A. (2019). How cells exploit tubulin diversity to build functional cellular microtubule mosaics. Curr. Opin. Cell Biol. *56*, 102–108.

23. Gadadhar, S., Bodakuntla, S., Natarajan, K., and Janke, C. (2017). The tubulin code at a glance. J. Cell Sci. *130*, 1347–1353.

24. Lacroix, B., Letort, G., Pitayu, L., Sallé, J., Stefanutti, M., Maton, G., Ladouceur, A.M., Canman, J.C., Maddox, P.S., Maddox, A.S., et al. (2018). Microtubule dynamics scale with cell size to set spindle length and assembly timing. Dev. Cell *45*, 496–511.e6.

25. Wilbur, J.D., and Heald, R. (2013). Mitotic spindle scaling during Xenopus development by kif2a and importin α. eLife *2*, e00290.

26. Reber, S.B., Baumgart, J., Widlund, P.O., Pozniakovsky, A., Howard, J., Hyman, A.A., and Jülicher, F. (2013). XMAP215 activity sets spindle length by controlling the total mass of spindle microtubules. Nat. Cell Biol. *15*, 1116–1122.

27. Kaye, B., Stiehl, O., Foster, P.J., Shelley, M.J., Needleman, D.J., and Fürthauer, S. (2018). Measuring and modeling polymer concentration profiles near spindle boundaries argues that spindle microtubules regulate their own nucleation. New J. Phys. *20*, 055012.

28. Decker, F., Oriola, D., Dalton, B., and Brugués, J. (2018). Autocatalytic microtubule nucleation determines the size and mass of *Xenopus laevis* egg extract spindles. eLife *7*, e31149.

29. Waterman-Storer, C.M., and Salmon, E.D. (1998). How microtubules get fluorescent speckles. Biophys. J. *75*, 2059–2069.

30. Nedelec, F., and Foethke, D. (2007). Collective Langevin dynamics of flexible cytoskeletal fibers. New J. Phys. *9*, 427.

31. Khan, I.A., and Ludueña, R.F. (1996). Phosphorylation of beta III-tubulin. Biochemistry *35*, 3704–3711.

32. Vemu, A., Atherton, J., Spector, J.O., Szyk, A., Moores, C.A., and Roll-Mecak, A. (2016). Structure and dynamics of single-isoform recombinant neuronal human tubulin. J. Biol. Chem. *291*, 12907–12915.

33. Pamula, M.C., Ti, S.C., and Kapoor, T.M. (2016). The structured core of human β tubulin confers isotype-specific polymerization properties. J. Cell Biol. *213*, 425–433.

34. Schindelin, J., Arganda-Carreras, I., Frise, E., Kaynig, V., Longair, M., Pietzsch, T., Preibisch, S., Rueden, C., Saalfeld, S., Schmid, B., et al. (2012). Fiji: an open-source platform for biological-image analysis. Nat. Methods *9*, 676–682.

35. Lamprecht, M.R., Sabatini, D.M., and Carpenter, A.E. (2007). CellProfiler: free, versatile software for automated biological image analysis. Biotechniques *42*, 71–75.

36. Grenfell, A.W., Strzelecka, M., Crowder, M.E., Helmke, K.J., Schlaitz, A.L., and Heald, R. (2016). A versatile multivariate image analysis pipeline reveals features of Xenopus extract spindles. J. Cell Biol. *213*, 127–136.

37. Nguyen, P.A., Field, C.M., Groen, A.C., Mitchison, T.J., and Loose, M. (2015). Using supported bilayers to study the spatiotemporal organization of membrane-bound proteins. Methods Cell Biol. *128*, 223–241.

38. Gardner, M.K., Charlebois, B.D., Jánosi, I.M., Howard, J., Hunt, A.J., and Odde, D.J. (2011). Rapid microtubule self-assembly kinetics. Cell *146*, 582–592.

39. Vemu, A., Garnham, C.P., Lee, D.Y., and Roll-Mecak, A. (2014). Generation of differentially modified microtubules using in vitro enzymatic approaches. Methods Enzymol. *540*, 149–166.

STAR★METHODS

KEY RESOURCES TABLE

REAGENT or RESOURCE	SOURCE	IDENTIFIER
Antibodies		
Anti-α-tubulin	SIGMA	Cat#: T5168, Clone B-5-1-2: RRID: AB_477579
Anti-β-tubulin	SIGMA	Cat#: T7816; RRID: AB_261770
Anti- αβ-tubulin	Cytoskeleton, Inc.	Cat#: ATN02; RRID: AB_10708807
Acetylated lysine 40 of α-tubulin	SIGMA	Cat#: T7451; RRID: AB_609894
Polyglutamylated tubulin	Adipogen	Cat#: gt335; RRID: AB_2490210
Tyrosinated C terminus of tubulin	Abcam	Cat#: ab6160; RRID: AB_305328
Tubulin C terminus with tyrosine removed	Abcam	Cat#: ab48389; RRID: AB_869990
Phosphorylated serine residues	Abcam	Cat#: ab9332; RRID: AB_307184
Anti-XMAP215	[26]	
HRP-conjugated goat anti-mouse	Proteintech Group	Cat#: 00001-1; RRID: AB_2722565
HRP-conjugated goat anti-rabbit	Proteintech Group	Cat#: 00001-2; RRID: AB_2722564
Chemicals, Peptides, and Recombinant Proteins		
Complete EDTA-free Protease Inhibitor Tablets	Roche	Cat#: 4693132001
Pregnant mare serum gonadotrophin	MSD, Tiergesundheit	Intergonan ® 240 IU/ml
Human chorionic gonadotrophin	SIGMA	Cat#: CG-10
Cytochalasin D	SIGMA	Cat#: C8273
Cycled bovine brain tubulin	PurSolutions	Cat#: 032005
Porcine brain tubulin	This paper	N/A
Xenopus laevis egg tubulin	This paper	N/A
Xenopus tropicalis egg tubulin	This paper	N/A
Bradford reagent	SIGMA	Cat#: B6916
Bacteriophage lambda phosphatase	Sigma-Aldrich	Cat#: P9614
Human PP2A-α/PP2AR complex	BPS Bioscience	Cat#: 30056
FastAP Thermosensitive Alkaline Phosphatase	ThermoFisher	Cat#: EF0651
Pluronic F-127	Sigma-Aldrich	Cat #: P2443
NeutrAvidin Protein	Thermo-Fisher	Cat #: 31000
κ-Casein from bovine milk	Sigma-Aldrich	Cat #: C0406
Dichlorodimethylsilane (DDS)	Sigma-Aldrich	Cat #: 440272
GMPCPP	Jena Bioscience	Cat #: NU-405L
Protocatechuic Acid (PCA)	Sigma-Aldrich	Cat #: 03930590
Protocatechuate-3,4-dioxygenase (PCD)	Sigma-Aldrich	Cat #: P8279
Trolox	Sigma-Aldrich	Cat #: 238813
Cy3 Mono NHS Ester	GE Healthcare	Cat #: PA13101
Cy5 Mono NHS Ester	GE Healthcare	Cat #: PA15101
Atto-488 NHS Ester	Atto-Tec	Cat #: AD 488-35
Critical Commercial Assays		
TOG columns	[17]	
PD10 desalting columns	GE Healthcare	Cat#: 17085101
Amicon®Ultra Centrifugal filters	Merck	Cat#: UFC8030
Protein G Dynabeads	Invitrogen	Cat#: 10009D
Pierce Glutathione Magnetic Agarose beads	Thermo Fisher	Cat#: 78601
Experimental Models: Organisms/Strains		
Xenopus laevis	Nasco	Cat#: LM00535
Xenopus tropicalis	Nasco	Cat#: LM00822

(Continued on next page)

Continued

REAGENT or RESOURCE	SOURCE	IDENTIFIER
Software and Algorithms		
NIS-Elements Advanced Research	Nikon	https://www.microscope.healthcare.nikon.com/en_EU/products/software/nis-elements/nis-elements-advanced-research
FIJI	[34]	https://imagej.net/Fiji/Downloads
CellProfiler	[35]	https://cellprofiler.org/releases/
Image analysis pipeline for spindles	[36]	https://rupress.org/jcb/article/213/1/127/38536/A-versatile-multivariate-image-analysis-pipeline
Cytosim	[30]	https://github.com/nedelec/cytosim
Prism version 8.0 for Mac OS X	GraphPad	https://www.graphpad.com/

LEAD CONTACT AND MATERIALS AVAILABILITY

Further information and requests for resources and reagents should be directed to and will be fulfilled by the Lead Contact, Simone Reber (simone.reber@iri-lifesciences.de). In general, plasmid constructs and antibodies are available for sharing.

EXPERIMENTAL MODEL AND SUBJECT DETAILS

The *Xenopus* frogs (adult females) used in this study are part of the *Xenopus* colony maintained at the animal husbandry of the Humboldt-Universität zu Berlin. Mature *X. laevis* and *X. tropicalis* frogs were obtained from NASCO (Fort Atkinson, WI). *Xenopus* frogs were maintained in a recirculating tank system with regularly monitored temperature and water quality (pH, conductivity, and nitrate/nitrite levels). *Xenopus laevis* were housed at a temperature of 18-20°C, and *Xenopus tropicalis* housed at 23-26°C. Frogs were fed with food pellets (V7106-0202) from ssniff Spezialdiäten GmbH. All experimental protocols involving frogs were performed in accordance with national regulatory standards and ethical rules and reviewed and approved by the LaGeSo under Reg.-Nr. 0096/15.

METHOD DETAILS

Purification of *Xenopus* egg tubulin

Cytostatic factor (CSF) extracts were prepared from *X. laevis* and X. tropicalis eggs arrested in metaphase of meiosis II as described previously [13]. Briefly, *X. laevis* frogs were primed with 100 U of pregnant mare serum gonadotrophin (PMSG) 3-7 days before the experiment and were boosted with 1000 U human chorionic gonadotrophin (HCG) to induce egg laying. *X. tropicalis* frogs on the other hand were primed with 10 U of HCG 16-24 hours and boosted with 200 U HCG 5 hours before the experiment to induce egg laying. Eggs arrested in the metaphase stage of meiosis II were collected, dejellied using L-Cysteine and fractionated via centrifugation. The cytoplasmic layer was isolated and supplemented with Cytochalasin D and Complete EDTA-free protease inhibitor. CSF-extract was kept on ice (*X. laevis*) or at room temperature (*X. tropicalis*) and was either used for spindle assembly reactions or for subsequent tubulin purification. Tubulin was purified as described in [17] using a fusion protein of GST and TOG domains 1 and 2 of *S. cerevisiae* Stu2 (GST-TOG1/2) coupled to a 5 mL HiTrap NHS-activated HP column (GE Healthcare). The extract was first diluted with an equal volume of BRB80 buffer (80 mM PIPES, 1 mM EGTA, 1 mM MgCl$_2$, pH 6.9) and centrifuged at 80,000 rpm in an MLA-80 rotor (Beckman-Coulter) for 10 min at 4°C. The supernatant was cycled through the column at 0.5 column volumes per minute (CV/min) for 20 min. The column was washed with 8 CV of BRB80 supplemented with 100 μM Mg^{2+} GTP (wash buffer) followed by 3 CV of BRB80 supplemented with 10 mM MgCl$_2$ and 5 mM ATP and incubated for 15 min to induce dissociation of chaperone proteins. The column was then washed with 3 CV BRB80/ATP buffer and 20 CV of wash buffer. Tubulin was eluted at 1 mL/min with wash buffer supplemented with 0.5 M (NH$_4$)$_2$SO$_4$. Peak fractions were determined by measuring A$_{280}$ values with a NanoDrop spectrophotometer (Thermo), pooled, buffer-exchanged into BRB80 containing 10 μM Mg^{2+} GTP using PD10 desalting columns (GE Healthcare) and concentrated to at least 30 μM using a concentration filter column with a 30 kDa cut-off (Amicon). Concentrated tubulin was incubated on ice for 30 min to fully depolymerize microtubules, centrifuged for 15 min at 2°C in a TLA-100 rotor at 80,000 rpm, aliquoted into 5 or 10 μl single-use aliquots, and snap-frozen in liquid nitrogen. Tubulin dimer concentration was determined by measuring absorbance at 280 nm with a NanoDrop. Purified tubulin was determined to be free of the major microtubule polymerase XMAP215 by Coomassie (Figure S1B) and free of other known MAPs and motors using mass spectrometry (see Table S1).

Tubulin activity measurements

Tubulin activity (Figure S1C) was assessed by polymerizing 20 μM tubulin in 1xBRB80 in the presence of 1 mM GTP and 33% v/v glycerol at 35°C for 40 min, layering the reaction on top of an equal volume of 1xBRB80 containing 60% glycerol, and centrifuging in a TLA100 rotor at 35°C for 10 min at 80,000 rpm. Polymerized microtubules form the pellet, whereas non-polymerized tubulin remains in the reaction mixture above the 60% glycerol layer. Relative tubulin abundance in the input, supernatant, and pellet fractions was assessed by SDS-PAGE and western blot analysis.

Spindle assembly reactions, imaging, and analysis

To promote bipolar spindle formation, demembranated sperm nuclei were added to undiluted CSF-extract, cycling to interphase was induced by the addition of $CaCl_2$ to 0.6 mM and after a 90 min incubation, the system was rearrested in M-phase using one volume of CSF-extract [13] followed by an additional incubation of 60 min. For the tubulin addition experiments, purified *X. laevis*, *X. tropicalis*, commercially available *B. taurus* tubulin (PurSolutions, Cat#: 032005) or buffer was added to the extract with preassembled spindles. All experiments were conducted at 20°C. Spindles were fixed in the presence of 0.2 mg ml^{-1} Cy3-labeled tubulin and DAPI in squash-fixed samples. Stacks of fixed spindles were acquired on a Nikon Eclipse Ti microscope with an Andor Spinning Disc Confocal (CSU-X) system attached. Images were acquired using a Nikon Plan Apo 100X/1.45 NA oil immersion objective lens and Andor iXon3 DU-888 Ultra camera, using the Nikon Elements software. Care was taken to ensure that the laser power and exposure time used for all imaging sessions was identical. Spindle length and total fluorescence intensity were quantified using FIJI [34] and an image analysis pipeline [36]. For each experiment, 60 spindles assessed over at least three different extracts were analyzed unless specified otherwise.

Depletion / add-back experiments and pull-down assays

Tubulin was pulled down from CSF-extracts using either Protein G Dynabeads (Invitrogen) coupled to anti-tubulin antibodies (α-tubulin clone b-5-1-2 (Sigma-Aldrich) / sheep polyclonal ATN02) or Pierce Glutathione Magnetic Agarose beads (Thermo Scientific) coupled to the recombinant GST-TOG1/2 protein. Coupling was performed by suspending beads in saturating concentrations of antibody or protein and incubating with gentle agitation at room temperature for 1 hour or overnight at 4°C. Beads were washed with CSF-XB (100 mM KCl, 0.1 mM $CaCl_2$, 2 mM $MgCl_2$, 5 mM EGTA, 50 mM sucrose, 10 mM HEPES, pH 7.7.), one volume of beads corresponding to ∼10% of the extract volume was used for extract depletion at 4°C for 30 min. The beads were then removed from the extract, washed with CSF-XB, and eluted with either SDS-PAGE loading buffer without DTT (antibody-coupled beads) or TOG column elution buffer (GST-TOG1/2-coupled beads). Fresh beads were added to the extract and this process was repeated for up to 4 rounds of depletion per extract sample. The amount of tubulin pulled down was evaluated by Coomassie and western blot.

Antibodies

A monoclonal anti-α-tubulin (SIGMA, T5168, Clone B-5-1-2) was used in western blots as a loading control. In addition, we used sheep polyclonal ATN02 also directed against α-tubulin and β-tubulin (Sigma T7816). K40: Acetylated lysine 40 of α-tubulin (Sigma Aldrich T7451 clone 6-11 B-1). Poly-Glu: Polyglutamylation of acidic residues (Adipogen gt335). Tyr: Tyrosinated C terminus of tubulin (Abcam ab6160). Detyr: Tubulin C terminus with tyrosine removed (Abcam ab48389). P-Ser: Phosphorylated serine residues (Abcam ab9332). The anti-XMAP215 antibody was raised against a peptide containing the last 15 amino acids of XMAP215 and affinity purified against this peptide as described before [26]. Secondary antibodies were HRP-conjugated anti-rabbit IgG (Proteintech 0001-2) and anti-mouse IgG (Proteintech 0001-1) from goat.

TIRF assays, image acquisition, and data processing

Flow chambers were constructed with glass coverslips passivated with dichlorodi-methylsilane [37] mounted onto glass slides using thin strips of parafilm. Chambers were functionalized by perfusing 20 μl of 100 μg/mL Neutravidin in BRB80 through the chamber and incubating for 5 min at room temperature. The chamber was rinsed twice with 20 μl BRB80, twice with a blocking buffer consisting of 1% w/v Pluronic F-127 (Sigma-Aldrich) in BRB80, and incubated at room temperature for 15 min. Wash buffer containing 1 mg/ml K-casein in BRB80 was flowed through the chamber followed by 2 × 20 μL of GMPCPP-stabilized microtubule seeds containing 10% Cy5-labled and 20% biotin-labeled tubulin suspended in wash buffer. Polymerization reactions were carried out at 37°C in BRB80 buffer supplemented with 1 mg/mL k-casein, 1% β-mercaptoethanol, 2 mM Trolox, 2.5 mM PCA, 25 nM PCD, and 0.15% methylcellulose at different concentrations of purified tubulin with 10% Cy3- or Atto488-labeled porcine brain tubulin. 50 μl of reaction solution were perfused through the chamber, then both ends were sealed with silicone grease. The slide was mounted on the objective and left for 10 min to allow the temperature to equilibrate before imaging with the exception of 9 μM reactions, which were imaged immediately in order to determine when steady state was reached (see Figure S3C). To measure microtubule dynamics in extract, BRB80 was replaced with CSF-XB and reactions were carried out at room temperature. Reactions contained 5 μL of egg extract, 0.5 μM vanadate, 0.5 μM Cy5-labeled tubulin, 0.15% methylcellulose, and were diluted in CSF-XB supplemented with 10% sucrose to a final volume of 20 μL. Images were taken on an inverted Nikon Eclipse Ti-E microscope with a motorized TIRF angle, a Nikon Plan Apochromat 100x/1.5NA oil immersion objective lens, and an Andor iXon Ultra X3 987 EMCCD camera or a Photometrics Prime 95B sCMOS camera. Atto488- labeled microtubules were imaged with a 488 nm laser, Cy3-labeled microtubules were imaged with a 561 nm laser and Cy5-labeled microtubule seeds were imaged with a 647 nm laser. Time-lapse images were taken at a frame rate of 0.2 fps with an exposure time of 500 or 700 ms. To measure microtubule dynamics in extract, images were acquired at 1 fps with an exposure time of 200 ms. Recording was controlled with the Nikon ND Acquisition software. Microtubule dynamics

were measured by producing kymographs using the Multi Kymograph function of the FIJI image analysis software [34] and manually fitting lines to growth and shrinkage events according to [38]. Growth and shrinkage velocities were calculated from the slopes of the fitted lines. Catastrophe frequencies were calculated as the inverse of the mean microtubule lifetimes, with the exception of *X. laevis* microtubules, where the catastrophe frequency was estimated as the total number of observed catastrophes divided by the total time microtubules spent in the growth phase. Rescue frequencies were calculated as the inverse of the mean duration of depolymerization events; events without a rescue were assigned a value of 0.

Simulation

We used Cytosim as described in [5, 16, 30]. Parameter values are summarized in Tables S2–S4. Spindle length was measured as the distance between the points of maximal NuMA density at the spindle poles. Microtubule length distribution was obtained from the recorded length of each individual microtubule (200 microtubules constant at any given state) at the end of the simulation. Microtubule mass was calculated by multiplying the lengths of all microtubules by 178.75 MDa [29].

Mass spectrometry

(1) For tubulin isoform composition (Figures 2A and 2B)

The isolated tubulins were analyzed using reverse-phase liquid chromatography–mass spectrometry (LC–MS). To analyze the purified tubulin via LC–MS, 2 μl of 5 μM tubulin were mixed with 10 μl of 0.1% trifluoroacetic acid (TFA) and centrifuged at 16,000 x g for 10 min at 4°C. The sample was loaded onto a Zorbax 300SB-C18 column (50 mm x 2.1 mm) (Agilent) attached in-line with an Agilent 6224 electrospray ionization time-of-flight LC–MS. A 0%–70% acetonitrile gradient in 0.05% TFA at a 0.2 ml/min flow rate was used. The data were analyzed using the Agilent Mass Hunter Workstation platform [39].

(2) For tubulin sample purity (Table S1)

Tubulin sample purity was evaluated by LC-MS/MS analysis of in-solution tryptic digests of purified tubulin aliquots. Digested samples were reconstituted in 20 μl of 0.05% TFA, 2% acetonitrile, 2 μl were analyzed by a reversed-phase nano liquid chromatography system (Ultimate 3000, Thermo Scientific) connected to an Orbitrap Velos mass spectrometer (Thermo Scientific). Samples were injected and concentrated on a trap column (PepMap100 C18, 3 μm, 100 Å, 75 μm i.d. x 2 cm, Thermo Scientific) equilibrated with 0.05% TFA, 2% acetonitrile in water. After switching the trap column inline, LC separations were performed on a capillary column (Acclaim PepMap100 C18, 2 μm, 100 Å, 75 μm i.d. x 25 cm, Thermo Scientific) at an eluent flow rate of 300 nl/min. Mobile phase A contained 0.1% formic acid in water, and mobile phase B contained 0.1% formic acid in acetonitrile. The column was pre-equilibrated with 3% mobile phase B followed by an increase of 3%–50% mobile phase B in 50 min. Mass spectra were acquired in a data-dependent mode using a single MS survey scan (m/z 350–1500) with a resolution of 60,000 in the Orbitrap, and MS/MS scans of the 20 most intense precursor ions in the linear trap quadrupole. The dynamic exclusion time was set to 60 s and automatic gain control was set to 1 × 106 and 5,000 for Orbitrap-MS and LTQ-MS/MS scans, respectively. Data processing and identification of proteins was performed using the Mascot Daemon software (version 2.5.0, Matrix Science). Processed spectra were used to search against the *X. laevis* protein database downloaded from Uniprot (Proteome ID UP000186698; last modified December 1, 2019). A maximum of three missed cleavages was allowed and the mass tolerance of precursor and sequence ions was set to 15 ppm and 0.35 Da, respectively. Methionine oxidation and acetylation (protein N terminus) were used as variable modifications and carbamidomethylation of cysteine residues was used as fixed modification. Only peptides with Mascot scores greater than the homology threshold were considered and a significance threshold of 0.05 was used based on decoy database searches. In addition, a peptide ion score cut-off of 20 was applied and only proteins with at least two significant sequences are reported in the output tables.

Phosphatase assays

3200 units of bacteriophage lambda protein phosphatase (Sigma-Aldrich) were mixed with 8 μg tubulin in either BRB80 or the supplied lambda protein phosphatase buffer (50 mM Tris-HCl pH 7.5, 100 μM Na$_2$ EDTA, 5 mM dithiothreitol, and 0.01% Brij 35) supplemented with 2 mM MnCl$_2$ and incubated at 30°C for 60 min. 25 units of alkaline phosphatase (FastAP Alkaline Phosphatase, ThermoFisher) were mixed with 11 μg tubulin in a 50 μL reaction in FastAP buffer (ThermoFisher) and incubated for up to 120 min at 37°C. Finally, 5.5 μg of tubulin were incubated with 2.1 μg of human PP2A-α/PP2AR complex (BPS Bioscience) in either BRB80 supplemented with 3 mM DTT or 20 mm HEPES, 100 mM NaCl, and 3 mM DTT, pH 7.2, for 60 min. For all reactions, phosphorylation status was evaluated by western blot using an anti-phosphoserine antibody.

QUANTIFICATION AND STATISTICAL ANALYSIS

In each figure legend, details about the quantifications have been provided, including the number of events/spindles measured (n), the mean/median values, and the SD/SEM. In addition, information about the statistical tests used for measuring significance and interpretation of p values is provided. For statistical analysis and plotting in this paper, we utilized Graphpad Prism version 8.0 for Mac OS X, GraphPad Software, La Jolla California USA, https://www.graphpad.com.

DATA AND CODE AVAILABILITY

The computational model was implemented in Cytosim, publicly available at https://github.com/nedelec/cytosim. The Cytosim version and meiotic spindle model specific to this study as in [5],[16]. Parameters that were used in the model, relating to Figures 4 and S4 have been indicated in Tables S2–S4. Please contact the Lead Contact for any further information regarding the code.